Research Article | Vol. 13, No. 12 / 1 Dec 2022 / Biomedical Optics Express 6621
Biomedical Optics EXPRESS

Decoherence of photon entanglement by transmission through brain tissue with Alzheimer's disease

E. J. GALVEZ,[1,*] B. SHARMA,[1] F. K. WILLIAMS,[1] C.-J. YOU,[1] B. KHAJAVI,[1] J. CASTRILLON,[1] L. SHI,[2] S. MAMANI,[3] L. A. SORDILLO,[3] L. ZHANG,[3] AND R. R. ALFANO[3]

[1]*Department of Physics and Astronomy, Colgate University, 13 Oak Drive, Hamilton, New York 13346, USA*
[2]*Department of Bioengineering, University of California-San Diego, 9500 Gilman Drive, La Jolla, California 92093, USA*
[3]*Institute for Ultrafast Spectroscopy and Lasers–Physics Department, The City College of New York, 160 Convent Avenue, New York, NY 10031, USA*
[*]*egalvez@colgate.edu*

Abstract: The generation, manipulation and quantification of non-classical light, such as quantum-entangled photon pairs, differs significantly from methods with classical light. Thus, quantum measures could be harnessed to give new information about the interaction of light with matter. In this study we investigate if quantum entanglement can be used to diagnose disease. In particular, we test whether brain tissue from subjects suffering from Alzheimer's disease can be distinguished from healthy tissue. We find that this is indeed the case. Polarization-entangled photons traveling through brain tissue lose their entanglement via a decohering scattering interaction that gradually renders the light in a maximally mixed state. We found that in thin tissue samples (between 120 and 600 micrometers) photons decohere to a distinguishable lesser degree in samples with Alzheimer's disease than in healthy-control ones. Thus, it seems feasible that quantum measures of entangled photons could be used as a means to identify brain samples with the neurodegenerative disease.

1. Introduction

Quantum entanglement is one of the most striking predictions of quantum theory. It relies on a delicate coherence in the state of two or more systems. Two particles entangled in one of their degrees of freedom (e.g., polarization for photons, or spin for electrons) exhibit striking non-local correlations in those degrees of freedom. If two particles are in a non-separable superposition of joint (product) states, operations on the state of one of the particles affect the state of both. The entanglement depends on a delicate coherence between the states that form the entangled state. Random perturbations to the system can degrade the coherence of the superposition, transforming it into a mixed state, or a statistical mixture of the possible product states. Apart from fundamental interest in the phenomenon, it begs the question of whether quantum entanglement can be harnessed for practical purposes.

Brain tissue consists of a web of organic components forming neurons, axons, embedded in an aqueous organic matrix. These contain cell components, such as membranes forming lipid bilayers, ion channels, and structural units, such as microtubules and proteins. Optically, this medium is inhomogeneous in matter concentration, locally birefringent but with no long-range optical order. Thus, light passage through it will experience a variety of transformations, such as scattering and dephasing, which depends on the type of neural organization (e.g., gray matter vs. white matter). Certain pathologies add new components to this matrix, such as proteins and tissue-modifying diseases, which may alter its interaction with light.

#474469 https://doi.org/10.1364/BOE.474469
Journal © 2022 Received 1 Sep 2022; revised 12 Nov 2022; accepted 13 Nov 2022; published 23 Nov 2022

Biomedical Optics EXPRESS

Classical polarimetry is a potential technique for distinguishing different types of tissue as they interact with the propagating light [1]. An important measure of this effect in the form of the Mueller matrix gives depolarization and dephasing information of classical light [2]. More recent efforts with classical non-separable superpositions of polarization and spatial modes are showing promise in optical biopsy [3]. An alternative test might be provided by quantum physics. Photons can contain a wealth of information. They can be in wavepackets that are superpositions of energy, momentum, polarization and spatial mode. When photon pairs are entangled in these degrees of freedom, a quantum form of coherence leads to non-local correlations. Our previous work showed that propagation through brain tissue does not quickly destroy this coherence [4]. Rather, it survives propagation through macroscopic distances. We found that as the light travels through the medium, it gradually loses its coherence. This gradual decoherence provides the potential for distinguishing between tissue types.

Two measures of the quantum state of entangled photons are the tangle, or the measure of non-separability of the quantum state, and the linear entropy, or the degree of mixture. These are not the only measures. There are other measures, such as concurrence, fidelity, von Neumann entropy, etc. These are determined by first measuring the quantum state of the light by quantum state tomography, which consists of a series of projective measurements that can be used to reconstruct the state of the light in the form of the density matrix [5]. The quantum measures can be extracted from the density matrix. Our previous work also showed that the passage of entangled photons through brain tissue decohered the state of the light along a specific route. If we plot the quantum-non-separability and state-mixing measures in the same plot: tangle (T) vs. linear entropy (S), we found that the state of the light follows the same path in this TS graph. The path is one that is known as the Werner state, where the state of the light converts directly from the highly coherent non-separable state gradually to a maximally mixed state [6,7]. The main hypothesis of this work is that the location of the state of the light along the Werner curve in the TS graph is a measure of the interaction of the non-classical light with the medium, and thus a quantum measure that can be used to distinguish between tissues affected by disease. In particular, our aim in this study is to distinguish in a quantitative way the presence of Alzheimer's disease (AD) in brain tissue.

Alzheimer's disease is a chronic neurodegenerative disease affecting a great portion of the aging population and usually leads to dementia. At the moment, there is no cure for it and therefore is invariably fatal [8]. There is neither a consensus about the causative factors for AD nor presence of unique hallmarks of physiopathologies. Two of the biggest contenders of a causative hypotheses are also present in the neuropathology of AD-afflicted brain tissue samples [9]. The first pathology is characterized by the presence of plaques outside and around the neurons (neuritic plaques) composed of insoluble amyloid-beta deposits. These deposits that contribute to the accumulation of the plaques are composed of misfolded amyloid beta protein. This aggregation of amyloid-proteins results in loss of synaptic plasticity in neural junctions [10]. The second pathology is characterized by the presence of neurofibrillary tangles which are aggregates of hyperphosphorylated tau protein. Neurons, like other cells have cytoskeletal structure which are partially supported by microtubules. The neuritic microtubules are stabilized when the tau protein is phosphorylated. However, in AD the tau proteins hyperphosphorylate, leading to the microtubules forming neurofibrillary tangles [11]. These structural changes may affect how light interacts with brain tissue.

This article is organized as follows. We continue with the theoretical background in Sec. 2, followed by Sec. 3 with the experimental method used in the research. Our results are presented in Sec. 4. Our conclusions are given in section 5.

Biomedical Optics EXPRESS

2. Transmission quantum state tomography

The technique consists of preparing pairs of photons in maximally-entangled Bell states in the polarization degree of freedom using spontaneous parametric down conversion. We did experiments with all 4 Bell states, but concentrated on the state that was most straight-forward to produce with our setup [12]:

$$|\psi\rangle = \frac{1}{\sqrt{2}}\left(|H\rangle_1|H\rangle_2 + |V\rangle_1|V\rangle_2\right), \tag{1}$$

where $|H\rangle$ and $|V\rangle$ denote the states of single photons with polarization aligned horizontally and vertically, respectively. Subindices correspond to the two photon modes. One of the photons was focused and sent through the brain-tissue sample. We then measured the state of the photons via quantum state tomography using a standard polarization projection technique [5]. The outcome was a 4×4 density matrix $\hat{\rho}$ representing the state of the light. We diagnosed the state of the light via various quantum measures [13]. More specifically, we focused on the tangle T and the linear entropy S. The former specifies the degree of entanglement, ranging from 0 for separable states to 1 for maximally non-separable states; the latter specifies the degree of mixture, ranging from 0 for pure states to 1 for maximal mixed states (i.e., a statistical superposition of all basis states with equal weights). They were used to display the degrees of non-separability and maximal mixture in a single graph of T *vs.* S [4]. We previously found that passage of light prepared and diagnosed in this way converts the entangled state into a state that is intermediate between maximally entangled and maximally mixed states, consistent with the Werner state [14], of density matrix given by

$$\hat{\rho}_w = p|\psi\rangle\langle\psi| + (1-p)\frac{\hat{I}}{4}, \tag{2}$$

where $\hat{I}$ is the identity, and p is the Werner probability [15].

Figure 1(a) shows the graph T vs. S for the Werner states. It includes labels with the value of p for points along the curve. Thus, the pair of values (S, T) locates the state in the graph.

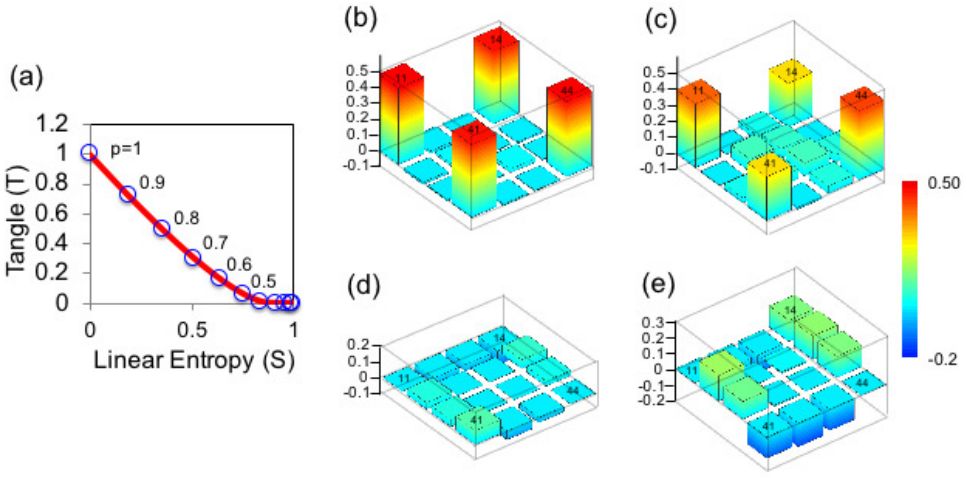

Fig. 1. (a) TS graph of Werner states; (b-e) Examples of tomographic measurements of data taken in this experiment. They show the bar-form of the real (b,c) and the imaginary components (d,e) of the density matrix of the light after one of the photons passed through 600-μm thick tissue with Alzheimer's disease (b,d) and control (healthy) (c,e). Color codes the magnitude of the elements and numbers on top of the tallest features denote the subindices (i,j) of the matrix element $\rho_{i,j}$.

Biomedical Optics EXPRESS

The value of p extracted from the data constitute a measure of the effect of the sample on the state of the light [14]. In Fig. 1(b-e) we show examples of two measured density matrices as displayed visually in the traditional bar-form, where the height of each bar represents the value of the real (b and c) and imaginary (d and e) components of the matrix elements, and the location, its position on the matrix. The density matrix for the initial Bell state of Eq. (1) consists of four bars of height 0.5 at the 4 corners with zero-height bars elsewhere including all imaginary components. The two sets of graphs show distinct metrics: $T = 0.83 \pm 0.07$ and $S = 0.12 \pm 0.10$ or $p = 0.94 \pm 0.04$ for (b and d); and $T = 0.45 \pm 0.07$ and $S = 0.38 \pm 0.08$ or $p = 0.77 \pm 0.04$ for (c and e). That is, the light shows nearly no decoherence and a high value of p for the case in (b and d), whereas it shows substantial decoherence and low value of p for the case in (c and e). More details on the significance of those results are given in Sec. 4.

3. Methods

3.1. Experimental apparatus

The apparatus is shown in Fig. 2. It consisted of three sections: a state preparation section, and interaction section, and a state-projection and measurement section. The state preparation section consisted of a pump diode laser of wavelength 405 nm and power 50-100 mW. The light went through a band-pass filter and Glan-Thompson polarizer to have a well-characterized beam. It was incident on a stack of two thin type-I BBO crystals (0.5 mm thick, 3-mm×3-mm in cross section) with their axes rotated 90 degrees relative to each other. That way the horizontal component of the pump laser produced vertical photon pairs in one crystal and the vertical component produced horizontal pairs in the other. The orientation of the pump beam was rotated by a half-wave plate to give equal detections of horizontally and vertically polarized photon pairs. The photon-path geometry made the crystal that originated the pair indistinguishable. Collection at narrow 3-degree angles from the input path gave negligible distinguishability due to walk-off. A tilted 8-mm thick quartz crystal placed between the half-wave plate and down-conversion crystals provided pre-temporal compensation to erase a 200 ps temporal distinguishability of the pairs produced in different crystals, plus phase adjustment, to obtain the state of Eq. (1).

In the interaction region, one of the photons was focused onto the sample using a 10× microscope objective, followed by a matching objective adjusted to refocus the maximum number of transmitted photons onto the fiber-optic collection components. The photons were focused onto the sample forming a roughly cylindrical region 20 μm in diameter and 100-600 μm in length (i.e., the sample thickness). We experimented with different geometries and focusing lenses, but the above mentioned was used for all the experiments presented here. For samples that were solid, such as brain tissue, the sample was on a vertical plane. For samples in suspension gravity would create a density gradient, so to have a uniform density across the sample we diverted the path so that the sample was on a horizontal plane, as shown in the insert to Fig. 2. Because doing a tomography required a significant amount of time (from tens of minutes to hours), we took multiple scans (7-12) of multiple positions in the samples, with integration times per projective measurement between 7 and 20 s.

In the measurement section of the apparatus, each photon of a pair traveled through a quarter-wave plate followed by a half-wave plate and a fixed Thompson-prism polarizer. After each Thompson prism was a 30-nm bandpass filter centered about 810 nm for detecting near-degenerate photon pairs. Past each filter was an optical fiber collimator that channeled the photons through multimode fibers to single-photon avalanche-diode detectors. The rotatable waveplates in conjunction with the fixed polarizers effectively projected the polarization state of the light onto any of the six main polarization eigenstates: linear horizontal, vertical, diagonal (+45° relative to horizontal), antidiagonal (−45° relative to horizontal), and right and left circular states. For convenience the waveplates were mounted on motorized mounts, so the measurement process

Biomedical Optics EXPRESS

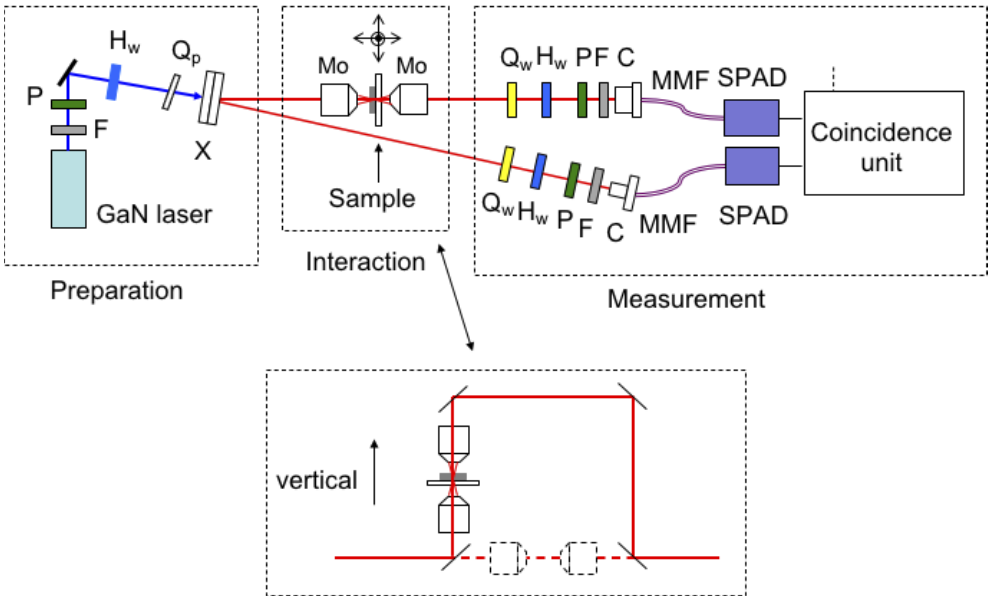

Fig. 2. Apparatus used in the experiment, split schematically in three sections. Polarization-entangled photon pairs were prepared in the first section via 405-nm photons from a GaN laser, and optical elements to adjust phase and temporal indistinguishability: Laser-line filter F, polarizer (P), Half-wave plate (H_w), quartz plate (Q_p) and down-conversion crystals (X). In the interaction region, one of the photons in a pair was focused onto the sample and the transmitted light was refocused by two ×10 microscope objectives (Mo). In the measurement section, each photon was projected onto a polarization state via quarter-wave plates (Q_w), half-wave plates (H_w) and fixed Thompson-prism polarizer (P). The photons were filtered by 40-nm bandpass filters (F) and launched into multimode fibers (MMF) with a collimator (C), and detected with a single-photon avalanche diode (SPAD). The electronic pulses from each detector were counted and by an electronic unit that also recorded coincident detections of photon pairs.

was fully automated. The photon detections were collected by an electronic unit that counted all counts plus coincident photon-pair detections within a time window of 40 ns.

The quantum efficiency of the detectors was about 60%, However, a host of optical elements in the path of the light toward its detection reduced this efficiency to below 10% in the photon path going through the tissue. To achieve consistent results and reliable signal to noise ratio, we had to integrate photon coincidence detections to at least 1000 counts. These low efficiencies also implied significant accidental coincidences, produced by the arrival of uncorrelated photons within the coincidence window. An estimate of the accidental count is obtained by $N_{\mathrm{acc}} = N_1 N_2 \Delta T / t_{\mathrm{dwell}}$, where N_1 and N_2 are the individual counts in each detector, ΔT the coincidence time window, and t_{dwell} the dwell time for each measurement. This estimate was subtracted from the data before the tomographic analysis. We put much care in taking data for both types of samples in identical conditions to avoid systematic errors. We measured the coincidence time in various ways to be sure we were subtracting a fair estimate. The results and conclusions of this work do not rest on this systematic correction. We used a standard quantum tomographic technique of 16 polarization-projective measurements, and optimized determination of the density matrix of the light [5].

Biomedical Optics EXPRESS

3.2. Samples

We investigated two types of samples: Post mortem human brain tissue samples and polystyrene spheres. The Post mortem human brain tissues from 6 subjects were analyzed. They include healthy brains as control (HC) and samples with Alzheimer's dementia (AD). The HC and AD brain tissues were obtained from the Human Brain And Spinal Fluid Resource Center and the Brain Endowment Bank UHealth-University of Miami Health System, respectively. We focused on three major brain regions: the hippocampus region and Broadmann's areas 9 and 17 of the cortex. Cubic brain tissues of dimensions 1-cm×1-cm×1-cm were fixed with 4% paraformaldehyde overnight at 4° C. The fixed brain tissues were sliced with vibratome into different thicknesses such as 120 μm, 500 μm, and 600 μm. The accuracy in tissue slice thickness was ±2 μm. The sliced samples were sealed in between glass slides, of dimension 3-in×1-in×1-mm, and coverslip. A spacer (double sided sticky) was sandwiched in between the glass slide and the coverslip to form the round shape well of 20-mm in diameter. Phosphate-buffered saline was added into the well to maintain the moisture as well as the intact tissue condition.

We used samples with polystyrene microspheres in various conditions to test the hypothesis that scattering is involved in the decoherence. We used microspheres with diameters 0.1 μm, 0.75 μm and 3 μm. They came in stock solutions with densities $N_{0.1\mu\text{m}} = 1.8 \cdot 10^{14}$ cm^{-3}, $N_{0.75\mu\text{m}} = 4.3 \cdot 10^{11}$ cm^{-3} and $N_{3\mu\text{m}} = 6.8 \cdot 10^{9}$ cm^{-3}, respectively. We further diluted them with deionized water and added surfactant by volume with ratios 1:1, 1:2 and 1:3. The diluted samples were prepared in separate vials, and 50 μL of that solution was transferred onto a microscope slide. The cells were made of several two-sided adhesive sample wells of 1 cm in diameter and thickness of 36 μm each. The sample in the well was sealed with cover slips. The cover slip perimeters were sealed with adhesive.

4. Results

4.1. Normal vs. Alzheimer's

Figure 3 shows one set of results. For slides with no sample we got results showing high entanglement. Shown in the figure, a representative data point (open triangle) with no sample is in the upper part of the Werner curve with $S = 0.02 \pm 0.07$ and $T = 0.96 \pm 0.04$, corresponding to $p = 0.98 \pm 0.03$. The remaining data in the graph shows results for samples with a thickness of 500 μm in different positions of the sample. We accumulated the data of consecutive scans to increase the signal to noise ratio. The data points for AD (lightly filled circles) are consistently higher along the Werner curve, with p in the range 0.87-0.98, whereas for the control sample (dark filled squares) the range is 0.71-0.88. That is, the data shows that the samples with AD impart lower decoherence onto the light than HC samples. Lower and higher thickness of samples resulted in the same pattern: data points spread along the Werner curve, with AD sample measurements higher along the curve than healthy samples.

In Table 1 we show a summary of all of our data. We have divided it into three sections of rows, depending on thickness. For the smallest thickness the difference is slight, as the differences in S, T and p can be seen to be within statistical error. Data at this thickness has been retaken many times (with several samples, testing different sites within each sample), always showing consistently AD samples higher than control ones. These results prompted us to consider investigating further at other thicknesses. The table's middle group, with a thickness of 500 μm, is also the data shown in Fig. 3. To avoid excessively long data runs for an entire tomographic run, resulting in long times separating early individual tomographic projection measurements from the final ones, we took data for shorter times and accumulated the data of consecutive runs. The last column shows the total time that was spent on each individual tomographic projection measurement. It can be seen that the results are independent on how much time is spent on a particular case; AD samples always show higher entanglement than HC ones. The third group

Biomedical Optics EXPRESS

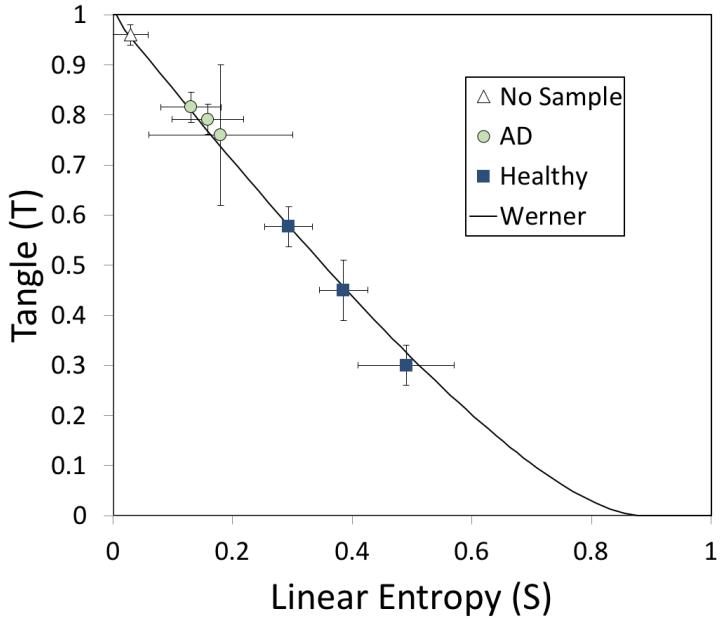

Fig. 3. Graph showing the quantum measures of tangle (T) and linear entropy (S) for the measurement of the state of polarization-entangled photons. One data point is representative of no sample, while other points are when one of the photons traveled through brain samples with a thickness of 500 μm. Two sets of samples involve subjects that suffered from Alzheimer's disease (AD) and healthy ones. The solid line corresponds to calculated outcomes for photons in Werner states where photons are partially in entangled and mixed states.

of measurements, at a larger thickness of 600 μm, show an even higher distinction between AD and HC samples. Figures 1(b,d) and 1(c,e) show the density matrix for AD and HC cases, respectively, for 600 μm samples. Already at the density-matrix stage of analysis the difference between the two types of samples is significant.

We also note that we did experiments with the other Bell states. These were encoded by adding two half-wave plates in the path of one of the photons. We prepared the states with waveplates set to angles (θ_1, θ_2) relative to the horizontal: $2^{-1/2}(|H\rangle_1|H\rangle_2 - |V\rangle_1|V\rangle_2)$ with $(0, \pi)$; $2^{-1/2}(|H\rangle_1|V\rangle_2 + |V\rangle_1|H\rangle_2)$ with $(0, \pi/4)$; and $2^{-1/2}(|H\rangle_1|V\rangle_2 - |V\rangle_1|H\rangle_2)$ with $(\pi, \pi/4)$. The tomographic results were independent of the state used, and so we did the bulk of the experiments with the state of Eq. (1), which required no additional waveplates. Adding two thick (6-mm thick) quartz plates in the path of one of the photons dephased/decohered the state into a mixed state giving data points that were low in the graph but slightly off the Werner curve, with $S = 0.68 \pm 0.02$ and $T = 0.008 \pm 0.005$. This is because they produced a mixed state of the $|H\rangle_1|H\rangle_2$ and $|V\rangle_1|V\rangle_2$ product states, and not a maximally mixed state involving also $|H\rangle_1|V\rangle_2$ and $|V\rangle_1|H\rangle_2$ states. The mixture of only $|H\rangle_1|H\rangle_2$ and $|V\rangle_1|V\rangle_2$ gives a theoretical linear entropy of 0.67, instead of 1 for a maximally mixed state. Thus, given that the data follows the Werner curve, we conclude that the entangled state follows a decoherence path towards a maximally mixed state.

4.2. *Polystyrene-sphere samples*

The brain samples described above do not absorb the light in any significant way. We hypothesized that the main physical process causing the decoherence is scattering. To confirm this we performed

Biomedical Optics EXPRESS

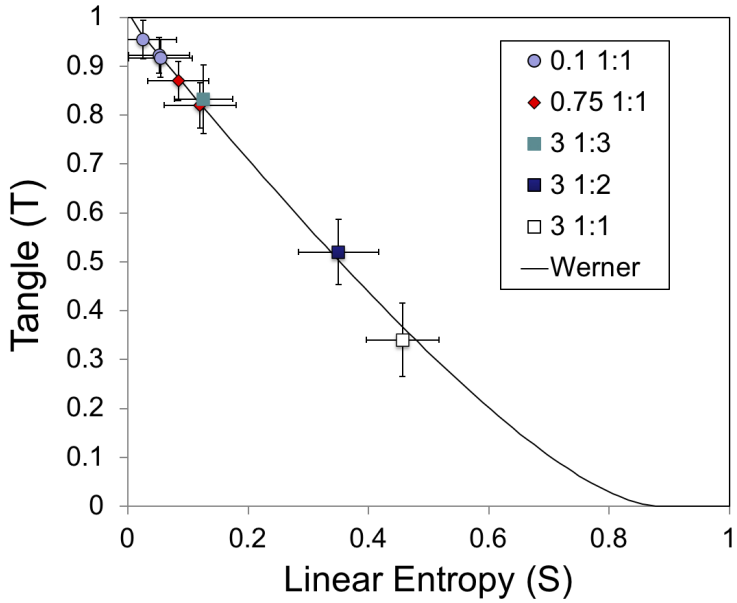

Fig. 4. Graph showing the quantum measures of tangle (T) and linear entropy (S) for the measurement of the state of polarization-entangled photons going through a sample of polystyrene spheres in suspension. Indicated are the values for different thickness and concentration in stock solution. The solid line corresponds to calculated outcomes for photons in Werner states where photons are partially in entangled and mixed states.

Table 1. Table showing a summary of the results of our tomographic measurements of human brain samples separated in groups of different thickness. They compare samples of subjects that suffered from Alzheimer's disease with those of healthy subjects. Tomographic measurements of the passage of the quantum state of entangled photons passing through the samples yielded quantum measures of tangle (T) and linear entropy (S), always appearing along the Werner curve (see Fig. 3). The location along the curve was quantified by the Werner probability p (Eq. (2)).

Sample Type	Thickness (μm)	Linear Entropy (S)	Tangle (T)	Werner Probability (p)	Total Time (s)
AD	120	0.17 ± 0.09	0.79 ± 0.09	0.91 ± 0.04	24
AD	120	0.15 ± 0.07	0.78 ± 0.08	0.92 ± 0.04	36
HC	120	0.16 ± 0.06	0.76 ± 0.06	0.91 ± 0.04	24
AD	500	0.18 ± 0.12	0.76 ± 0.14	0.90 ± 0.07	72
AD	500	0.13 ± 0.05	0.82 ± 0.03	0.93 ± 0.03	77
AD	500	0.16 ± 0.06	0.79 ± 0.03	0.92 ± 0.03	150
HC	500	0.49 ± 0.08	0.30 ± 0.04	0.71 ± 0.03	120
HC	500	0.39 ± 0.04	0.45 ± 0.06	0.78 ± 0.03	40
HC	500	0.29 ± 0.04	0.58 ± 0.04	0.84 ± 0.02	60
AD	600	0.12 ± 0.10	0.83 ± 0.06	0.92 ± 0.04	36
HC	600	0.39 ± 0.07	0.47 ± 0.06	0.79 ± 0.04	18
HC	600	0.38 ± 0.08	0.45 ± 0.07	0.79 ± 0.04	48

Biomedical Optics EXPRESS

similar tomographic measurements of samples of polystyrene spheres, as described in Sec. 3.2. The data for all the different types of samples with different sphere diameters and dilutions is consistent: all points fall closely along the Werner curve, as seen in Fig. 4. The error bars were calculated by error propagation of the quantum measures. From the way they show in the graph, these uncertainties seem to be an overestimate. More importantly, it is consistent with the hypothesis that scattering produces the same type of decoherence that is observed with the tissue samples.

5. Conclusions

We summarize our results as follows. Photons transmitted through brain tissue experience a decohering process consistent with transformation of a fully entangled state into a maximally mixed state. This is consistent with our previous results [4]. Further tests with polystyrene spheres in suspension makes a case that the main mechanism for the quantum decohering process is scattering. Our tests of brain tissue samples from subjects with Alzheimer's disease convincingly show a difference with control samples from healthy subjects. One might expect that a transformative disease like Alzheimer's would induce a greater transformation on the state of the light. However, we found the opposite: samples with Alzheimer's preserve the entanglement to a distinguishable degree over healthy samples.

Previous research on Alzheimer's *versus* normal tissue of mouse brain showed that samples with Alzheimer's produced higher scattering than normal tissue [16,17]. This seems to be a discrepancy with our findings. However, the techniques used in both studies (3μm thick samples in Ref. [16], and backscattering measurements in Ref. [17]) make those works sensitive to Rayleigh scattering, where scattering irregularities are smaller than the wavelength. Our study, with much thicker samples and collecting mostly scattering into a forward cone, is more sensitive to Mie scattering, where scatterers are larger than the wavelength. In any case, the discrepancy warrants further investigation.

Beyond the sets of measurements presented here, quantum decoherence could be used as an imaging parameter. With technologies for imaging single photons now available, it should be possible to create images of tissue where the variable parameter is the Werner probability or an equivalent quantum measure. Such measurements could potentially give new information of use in the study of disease. Our studies are restricted to transmission of light through tissue. We were not able to do similar studies of reflection because of low signal to noise ratio. However, our source of entangled photons is a modest one, using thin type-I BBO crystals. Brighter sources of polarization-entangled photons using long periodically poled materials, such as PPKTP, are available [18]. Should reflection techniques give positive results, they may enable in-vivo detection of Alzheimer's by sensing of the retina, where previous studies have found the presence of amyloid-beta and hold promise for early detection of Alzheimer's disease [19–22]. The advantage of single photons over other techniques is that they involve femto-watt powers, which would not do tissue damage.

Funding. National Science Foundation (PHY-1506321, PHY-2011937); Colgate University Picker Interdisciplinary Science Institute; Army Research Office (W911NF-19-1-0373).

Disclosures. The authors declare no conflicts of interest.

Data availability. Data underlying the results presented in this paper are not publicly available at this time but may be obtained from the authors upon reasonable request.

References

1. M. Sun, H. He, N. Zeng, E. Du, Y. Guo, S. Liu, J. Wu, Y. He, and H. Ma, "Characterizing the microstructures of biological tissues using Mueller matrix and transformed polarization parameters," Biomed. Opt. Express **5**(12), 4223–4234 (2014).
2. B. Cameron, Y. Li, and A. Nezhuvingal, "Determination of optical scattering properties in turbid media using Mueller matrix imaging," J. Biomed. Opt. **11**(5), 054031 (2006).

Biomedical Optics EXPRESS

3. S. Mamani, L. Shi, T. Ahmed, R. Karnik, A. Rodríguez-Contreras, D. Nolan, and R. Alfano, "Transmission of classically entangled beams through mouse brain tissue," J. Biophotonics **11**(12), e201800096 (2018).
4. L. Shi, E. Galvez, and R. Alfano, "Photon entanglement through brain tissue," Sci. Rep. **6**(1), 37714 (2016).
5. D. James, P. Kwiat, W. Munro, and A. White, "Measurement of qubits," Phys. Rev. A **64**(5), 052312 (2001).
6. A. G. White, D. F. V. James, W. J. Munro, and P. G. Kwiat, "Exploring Hilbert space: accurate characterization of quantum information," Phys. Rev. A **65**(1), 012301 (2001).
7. G. Puentes, A. Aiello, D. Voigt, and J. P. Woerdman, "Entangled mixed-state generation by twin-photon scattering," Phys. Rev. A **75**(3), 032319 (2007).
8. NIH, National, and I. on Aging (NIA), Alzheimer's disease fact sheet, https://www.nia.nih.gov/health/alzheimers-disease-fact-sheet.
9. M. A. DeTure and D. W. Dickson, "The neuropathological diagnosis of Azheimer's disease," Mol. Neurodegener. **14**(1), 32 (2019).
10. G. K. Gouras, T. T. Olsson, and O. Hansson, "β-amyloid peptides and amyloid plaques in Alzheimer's disease," Neurotherapeutics **12**(1), 3–11 (2015).
11. L. I. Binder, A. L. Guillozet-Bongaarts, F. Garcia-Sierra, and R. W. Berry, "Tau, tangles, and Alzheimer's disease," Biochim. Biophys. Acta, Mol. Basis Dis. **1739**(2-3), 216–223 (2005).
12. P. Kwiat, E. Waks, A. White, I. Appelbaum, and P. Eberhard, "Ultrabright source of polarization-entangled photons," Phys. Rev. A **60**(2), R773–R776 (1999).
13. J. Altepeter, E. Jefrey, and P. Kwiat, "Photonic state tomography," Adv. At., Mol., Opt. Phys. **52**, 105–159 (2005).
14. E. Galvez, B. Sharma, F. Williams, B. Khajavi, and L. Shi, "Transmission quantum state tomography of biological tissue," Asian J. Phys **29**, 379–386 (2020).
15. R. Werner, "Quantum states with Einstein-Podolsky-Rosen correlations admitting a hidden-variable model," Phys. Rev. A **40**(8), 4277–4281 (1989).
16. M. Lee, E. Lee, J. Jung, H. Yu, K. Kim, J. Yoon, S. Lee, Y. Jeong, and Y. Park, "Label-free optical quantification of structural alterations in Alzheimer's disease," Sci. Rep. **6**(1), 31034 (2016).
17. M. Borovkova, A. Bykov, A. Popov, A. Pierangelo, T. Novikova, J. Pahnke, and I. Meglinski, "Evaluating β-amyloidosis progression in Alzheimer's disease with Mueller polarimetry," Biomed. Opt. Express **11**(8), 4509–4519 (2020).
18. Z. Levine, J. Fan, J. Chen, and A. Migdall, "Polarization-entangled photon pairs from a periodically poled crystalline," Opt. Express **19**(7), 6724–6740 (2011).
19. M. C. W. Campbell, L. J. F. Gowing, Y. Choi, and Z. Leonenko, "Imaging of amyloid-beta deposits in the postmortem retina in Alzheimer's disease," Investigative Ophthalmology & Visual Science **51**, 5778 (2010).
20. M. Koronyo-Hamaoui, Y. Koronyo, A. V. Ljubimov, C. A. Miller, M. K. Ko, K. L. Black, M. Schwartz, and D. L. Farkas, "Identification of amyloid plaques in retinas from Alzheimer's patients and noninvasive in vivo optical imaging of retinal plaques in a mouse model," NeuroImage **54**, S204–S217 (2011).
21. Y. Qiu, T. Jin, E. Mason, and M. C. W. Campbell, "Predicting thioflavin fluorescence of retinal amyloid deposits associated with Alzheimer's disease from their polarimetric properties," Trans. Vis. Sci. Tech. **9**(2), 47 (2020).
22. P. J. Snyder, J. Alber, C. Alt, L. J. Bain, B. E. Bouma, F. H. Bouwman, D. C. DeBuc, M. C. W. Campbell, M. C. Carrillo, E. Y. Chew, M. F. Cordeiro, M. R. Due nas, B. M. Fernández, M. Koronyo-Hamaoui, C. La Morgia, R. O. Carare, S. R. Sadda, P. van Wijngaarden, and H. M. Snyder, "Retinal imaging in Alzheimer's and neurodegenerative diseases," Alzheimer's Dementia **17**(1), 103–111 (2021).